

# Mechanism study of TADF and phosphorescence in dinuclear copper (I) molecular crystal using QM/MM combined with an optimally tuned range-separated hybrid functional

Lingling Lv<sup>a,b,\*</sup>, Kun Yuan<sup>a,b</sup>, Changdai Si<sup>a</sup>, Guofang Zuo<sup>a</sup>, Yongcheng Wang<sup>c</sup>

<sup>a</sup> College of Chemical Engineering and Technology, Tianshui Normal University, Tianshui, Gansu, 741001, China

<sup>b</sup> Supercomputing Center for Theoretical Chemistry, Tianshui Normal University, Tianshui, Gansu, 741001, China

<sup>c</sup> College of Chemistry and Chemical Engineering, Northwest Normal University, Lanzhou, Gansu, 730070, China

## ARTICLE INFO

### Keywords:

Cu<sub>2</sub>I<sub>2</sub>(P<sup>+</sup>N)<sub>3</sub>

TADF and phosphorescence

Thermal vibration correlation function

ONIOM model

## ABSTRACT

Investigations of the detailed photophysical processes are of great significance for future material improvements and novel designing strategies. Herein, the interconversion and decay rates of the first excited singlet state (S<sub>1</sub>) and triplet state (T<sub>1</sub>) for the Cu<sub>2</sub>I<sub>2</sub>(P<sup>+</sup>N)<sub>3</sub> complex are calculated using the thermal vibration correlation function (TVCF) theory, combined with the optimally tuned range-separated hybrid functional (OT-ωB97XD) method at different temperature. A methodology with the building different ONIOM models, was carried over into simulation of crystal environment. All calculated results perfectly match the experimentally available data, demonstrating the validity of our applied theoretical approach. It has been found that the reverse intersystem crossing (RISC) rate  $k_{\text{RISC}}$  from T<sub>1</sub> to S<sub>1</sub> is  $3.11 \times 10^{10} \text{ s}^{-1}$  at 300 K, about 7 order of magnitude larger than the phosphorescence rate  $k_{\text{r}}(\text{T}) = 3.71 \times 10^3 \text{ s}^{-1}$ , and far more than ISC rate  $k_{\text{ISC}}(\text{T}_1\text{-S}_0)$  of  $6.38 \text{ s}^{-1}$ . The S<sub>1</sub> state can be an efficient thermal population from the T<sub>1</sub> state by the RISC pathway, leading to an occurrence of thermally activated delayed fluorescence (TADF), and the estimated delayed time of  $\tau(\text{TADF}) = 10 \mu\text{s}$ . On the other hand, the T<sub>1</sub> state also exhibits stronger admixtures with higher lying singlet states due to stronger SOC, having a larger ZFS of  $17 \text{ cm}^{-1}$ , thus, a relatively fast phosphorescence decay rate of  $k_{\text{r}}(\text{T}) = 8.542 \times 10^3 \text{ s}^{-1}$  estimated by Einstein emission formula is observed. Further calculation results show that the emission intensities are stemming by 91% from the S<sub>1</sub> state as TADF and by 9% as phosphorescence from the T<sub>1</sub> state at 300 K, which indicates the ambient temperature emission represents the combined luminescence of TADF and phosphorescence. Our work would be useful for improving and designing the luminescent material combined high-efficiency TADF with phosphorescence.

## 1. Introduction

In recent years, the thermally activated delayed fluorescence (TADF) materials as the third-generation emitters have attracted great attentions because this is driven by high values of commercial applications, especially in the fields of electroluminescence, for instance organic light emitting diodes (OLED) [1–4]. The OLED market is estimated to reach the \$30 billion mark by the end of 2018 [3]. But, almost three decades ago, people generally recognized that the OLED emitters are the second-generation of OLED, which employs triplet harvesting effect instead of fluorescent ones. In other words, the lowest triplet state (T<sub>1</sub>) can be easily populated from their excited singlet states by fast ISC (intersystem crossing) with the help of efficient spin-orbit coupling

(SOC) interaction, which can lead to relatively high radiative rates of transitions from the T<sub>1</sub> state to the singlet ground state (S<sub>0</sub>). In this case, third row transition metal complexes with Ir(III), Pt(II), and Os(II) central metal ions are well satisfied for such processes. Moreover, this strategy appears to be particularly successful in treating the red and green light emitting OLEDs. However, the disadvantages of this second-generation OLED also show obvious [5,6]: on the one hand, their rather long radiative lifetimes lead to quenching processes and bleaching reactions owing to higher lying metal centered d-d\* states; on the other hand, these pricey transition metals, such as Ir, Pt, and Os etc. not only are considerably costly but also have toxicity. With the increasing of OLED utilization, costs of production become an important factor to be considered.

\* Corresponding author. College of Chemical Engineering and Technology, Tianshui Normal University, Tianshui, Gansu, 741001, China.

E-mail address: [lvling002@163.com](mailto:lvling002@163.com) (L. Lv).

<https://doi.org/10.1016/j.orgel.2020.105667>

Received 9 December 2019; Received in revised form 4 February 2020; Accepted 18 February 2020

Available online 27 February 2020

1566-1199/© 2020 Elsevier B.V. All rights reserved.

To overcome these shortcomings, one can focus on the exploration of the new-generation emitters with the TADF characters. The TADF phenomenon was first discovered by Perrin in 1929 and obtained a rapid development since Adachi and co-workers adopted a promising TADF strategy, to design purely organic TADF emitters and successfully applied such emitters in the active layers of OLEDs in 2012 [5,7]. For the TADF emitters, it is well known that efficient TADF must satisfy the vital condition of a rather small excited singlet-triplet energy gap that lies within the range of thermal energy at room temperature, which leads to a thermally activated reverse (up-conversion) intersystem crossing (RISC) from the triplet manifolds  $T_1$  ( $M_s=0, \pm 1$ ) to the  $S_1$  state. The singlet excitons reproduced in the ways from the 75% of the  $T_1$  state excitons can then decay radiatively to the  $S_0$  state, which causes a delayed fluorescence signal that can compensate the prompt fluorescence, and so called the TADF, leading to the theoretical maximum quantum yield of up to 100%, these processes are showed in Fig. 1 [8,9].

As is well known, it is desired to find a compromise strategy that materials are neither expensive nor toxic, and appropriate for TADF mechanism. Interestingly, Cu(I) complexes as a promising emitter class came into the focus of the academic and commercial communities [10]. Compared to those  $d^6$  and  $d^8$  metal complexes, the Cu(I)  $d^{10}$  metal complexes often have smaller SOC. Therefore the  $T_1 \rightarrow S_0$  transition is largely spin-forbidden, and this results in emission decay times of several hundred microseconds. On the other hand, they generally have a small energy gap  $\Delta E(S_1-T_1)$  between the  $S_1$  and  $T_1$  states and a stable  $T_1$  state, because their excited states,  $S_1$  and  $T_1$ , often indicate low-lying metal to ligand charge transfer (MLCT) characters. In this situation, a noticeable charge separation between the metal and ligand upon excitation will lead to the small quantum exchange interaction, namely the smaller singlet-triplet splitting,  $\Delta E(S_1-T_1)$ . Therefore a TADF process becomes possible.

Recently, in order to design excellent Cu-based TADF materials, some theoretical and experimental groups have carried out the corresponding studies. Marian and co-workers have reported that the photophysical properties of a three-coordinate Cu(I) complex with a

monodentate N-heterocyclic carbene (NHC) ligand and a heterocyclic bidentate ligand [11]. In 2019, Luminescent of linear N-heterocyclic carbene copper(I) pyridine complexes investigated using a combination of spectroscopy and density functional theory (DFT)/time-dependent DFT (TD-DFT) calculations by Föller and Marian was found that this structural motif was very favorable for generating excited triplet states with high MLCT excitations and the RISC process was much faster than submicrosecond fluorescence by two orders of magnitudes [12]. Subsequently, Shuai and Peng groups also studies the photophysical properties of two-coordinate copper(I) complexes by the hybrid quantum mechanics and molecular mechanics (QM/MM) method with thermal vibration correlation function rate theory in solution and solid phase [13]. Cui et al. reported in detail the TADF phenomenon of two copper (I) complexes with 5-(2-pyridyl)-tetrazolate and phosphine ligands in gas, solution, solid phases employing the ONIOM approach [14]. Our team also explored the TADF properties for a series of the copper(I) complexes in different environments by using the accurate quantum calculation methods and obtained some valuable conclusions for material design [15–17]. In terms of experiments, Yersin and his group, as a typical representative of studying the Cu(I) complexes with TADF performance, synthesized a series of the TADF copper complexes and deduced a wealth of valuable experimental data and photophysical mechanism using the spectral technology [10,18]. Very recently, the luminescent properties of the three-fold di-nuclear Cu(I) complex of  $\text{Cu}_2(\mu\text{-I})_2(1\text{N-n-butyl-5-diphenyl-phosphino-1,2,4-triazole})_3$ ,  $\text{Cu}_2\text{I}_2(\text{P}^*\text{N})_3$  (see Fig. 2) have been reported by Yersin et al. [19], and yet  $\text{Cu}_2\text{I}_2(\text{P}^*\text{N})_3$  was synthesized and purified as reported in ref. 20 [20]. They exhibit highly efficient TADF as well as phosphorescence at ambient temperature with a total quantum yield of 85% for the powder material. Although the radiative rates of the excited singlet and triplet states, zero-field splitting (ZFS) as well as  $\Delta E(S_1-T_1)$  were measured by fitting according to the experimental data, the details of excited state processes, such as radiative or nonradiative decay rates, ISC and RISC rates between excited singlet and triplet states, remain unclear. Therefore the detailed photophysical processes are worth further theoretical calculations for material improvements and new design strategies. To our knowledge, this work has not been done to theoretically reveal the strong TADF mechanism in solid state for the three-fold di-nuclear Cu(I) complexes.

Driven by motives of these questions, theoretical calculations will help to achieve a better understanding of the detailed decay processes and electronic structures of excited states for such compounds. However, a reliable and efficient calculation approach for the prediction of these problems is essential, as it would help to determine the origin of experimental results as far as possible. Currently, there are two large challenges to be able to accurately describe the charge transfer (CT) excited state properties of TADF emitters and the solid environment in theoretical studies. In this work, the CT excited states have been dealt with the range-separated (RS) exchange density functional (e.g.  $\omega\text{B97XD}$  and  $\text{CAM-B3LYP}$ ) combined with tuning  $\omega$  (range-separation parameter) via the nonempirical procedure [21–23]. Recently, the introduction of an appropriate, fixed amount of exact-exchange (eX) functional has been demonstrated to provide an improved description of the CT excited-state. Another key challenge in the computational model of TADF is the description of solid environmental effects. In this study, we systematically and quantitatively studied on the excited state decay dynamics for the three different models in solid state environment by applying a popular layered ONIOM approach combined with a thermal vibration correlation function (TVCF) theory developed by Shuai's group [24,25], which provides a quantitative understanding. These deep investigation of luminescence mechanism is very meaningful for the molecular design of novel highly efficient dinuclear Cu(I) complexes.

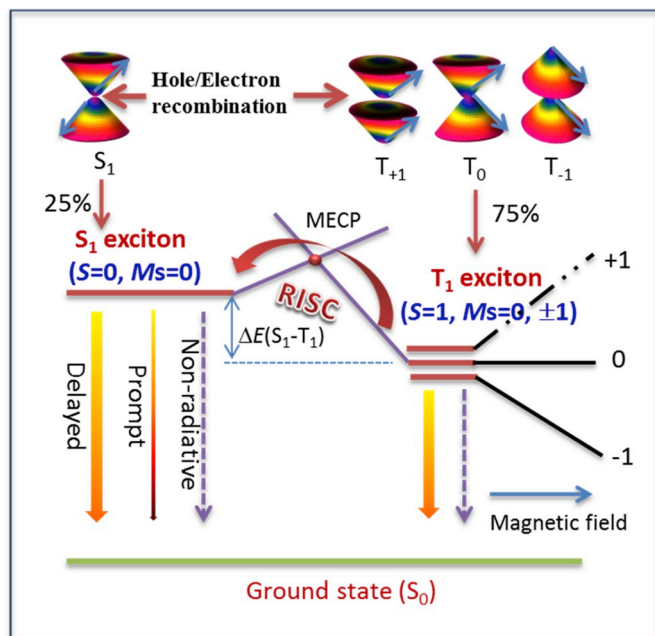


**Fig. 1.** Photophysical processes of generated excitons for fluorescence, thermally active delayed fluorescence and phosphorescence in the TADF molecules. RISC and MECP represent reverse intersystem crossing, and minimum energy crossing point, respectively; schematic vector representation of a triplet state ( $T_1$ ) with spin magnetic quantum number ( $M_s = 0, \pm 1$ ) and a singlet state ( $S_1$ ) with  $M_s = 0$ .

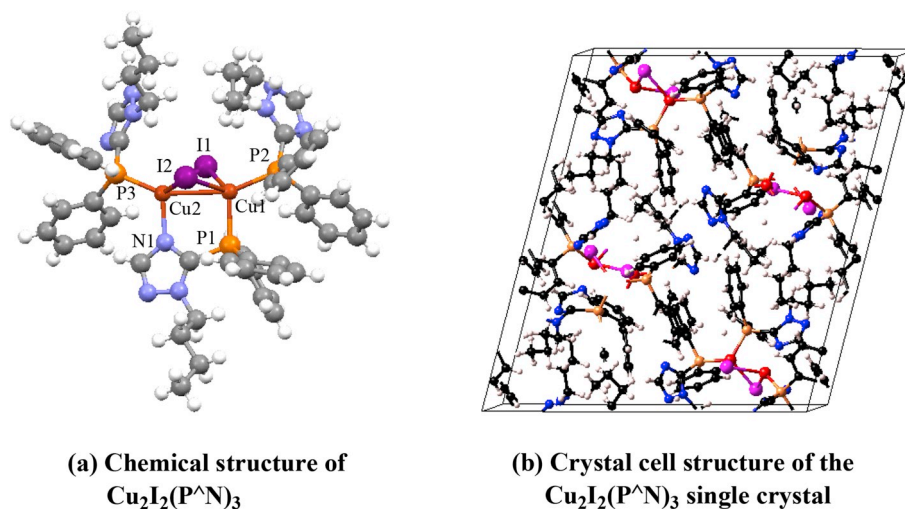


Fig. 2. Chemical and crystal cell structures of  $\text{Cu}_2\text{I}_2(\text{P}^{\wedge}\text{N})_3$  ( $\text{Cu}_2(\mu\text{-I})_2(1\text{N-n-butyl-5-diphenyl-phosphino-1,2,4-triazole})$ ).

## 2. Computation details

### 2.1. Calculation model construction

The aggregation effect of the crystal phase of the  $\text{Cu}_2\text{I}_2(\text{P}^{\wedge}\text{N})_3$  molecule is simulated by the two-layer ONIOM model that is constructed according to the X-ray crystal structure [20], and the detail packing clusters are plotted in Fig. 3. As can be seen from Fig. 3, three different models are constructed using a two-level ONIOM model theory to verify the influence of the different aggregation models on the photophysical processes, where are a centered  $\text{Cu}_2\text{I}_2(\text{P}^{\wedge}\text{N})$  molecule as high layer with 130 atoms, and surrounding remaining molecules considered as low layer level. Namely, Mod 1 is a 2-dimensional model ( $3 \times 3 \times 1$ ), low layer of 1040 atoms; low layer of 3120 atoms for Mod 2 with the size of  $5 \times 5 \times 1$ ; and Mod 3 is 3-dimensional model of the  $3 \times 3 \times 3$  size with the low layer of 3380 atoms. In the ONIOM calculations, the central molecule is treated using the accurate high-level QM method, while the outermost molecules as MM part are calculated using the efficient universal force field (UFF) method [26], and this part are frozen during the ONIOM geometry optimizations. Moreover, the MM charges are computed using the QEQ formalism that is embedded onto the QM electronic structure to consider the polarization interaction of the MM charges on the QM atoms [27]. All these ONIOM calculations were carried out with the Gaussian 09 program [28].

### 2.2. Geometry optimizations

Periodic calculations have been carried out using the plane-wave technique as implemented in the Vienna ab initio simulation package (VASP) code using the projector augmented wave pseudopotential for the core electrons [29]. The exchange correlation potential was described by employing the generalized gradient approximation (GGA) with Perdew-Burke-Ernzerhof (PBE) functional with a 500 eV cutoff energy for the plane wave basis set for the valence electrons [30]. Spin-polarized calculations were performed.

At the beginning of calculations, the B3LYP is chosen as the QM initial approach for geometric optimizations of the ground state in the ONIOM calculations. As for the excited state optimization, the TD-DFT theory is a useful and reliable tool to explore the excited states of relatively large molecular systems. But, the precise descriptions of the excited state properties are strongly dependent on the choice of functional in the framework of TD-DFT, especially, for the description and optimization of CT excited states. The standard functionals may fail completely in predicting the excitation energies when computing such large CT systems. Fortunately, the RS exchange density functional can

improve the description of the CT properties due to putting up with the incorrect asymptotic behavior in the long-range limit. The general formula of the RS functionals can be defined as follows equation (1) [21–23].

$$\frac{1}{R_{12}} = \frac{1 - [\alpha + \beta \text{erf}(\omega R_{12})]}{R_{12}} + \frac{\alpha + \beta \text{erf}(\omega R_{12})}{R_{12}} \quad (1)$$

herein, according to the error function (erf), the double electron repulsion operator  $1/R_{12}$  is divided into two types by means of Ewald-style partition: a short-range interaction with the first term on the right-hand side described by DFT exchange potential and a long-range interaction with the second term described by the HF exchange integral. The  $\omega$  of range-separation parameter, in unit of  $\text{Bohr}^{-1}$ , reveals the exchange terms switches from DFT to HF as the distance of  $R_{12}$  changes between the electrons at the coordinate vectors  $R_1$  and  $R_2$ . The “optimal tuning” amounts to the optimization of the  $\omega$  parameter, which was performed by the optDFTw procedure under the B3LYP optimized geometries, on the basis of the exact Kohn-Sham theory [31]. This theory indicates that the negative HOMO energy for an N-electron system equals to the vertical ionization potential, as shown in formula 2. The optimally-tuned RS functional of  $\omega\text{B97XD}$  for three modes of  $\text{Cu}_2\text{I}_2(\text{P}^{\wedge}\text{N})_3$  is carried out to obtain the optimal  $\omega$  values when  $J^2$  reaches the minimum, and marked as “OT- $\omega\text{B97XD}$ ”, the  $\omega$  results are depicted as in Fig. 4.

$$J^2 = \sum_{i=0}^1 [\epsilon_{\text{H}}(\text{N} + i) + IP(\text{N} + i)]^2 \quad (2)$$

The  $S_0$  and  $T_1$  states were then reoptimized using the optimal  $\omega$  values for the QM region of the ONIOM high-layer, and the calculations were also implemented by the popular non-optimized CAM-B3LYP functional including a finite amount of short-range exchange, namely as  $\alpha = 0.2$  for comparison [32]; and the  $S_1$  states were optimized by using the time-dependent OT- $\omega\text{B97XD}$  functional. In all DFT and TD-DFT calculations, the SDD pseudo-potential basis set is applied for the I atom and 6–31+ G(d) basis set is applied to the remaining other atoms.

Finally, harmonic vibrational analyses in the solid phase are calculated using the same ONIOM computational level. These vibrational frequencies and modes are applied to the subsequent TVCF calculations.

### 2.3. Calculations of electronic structures

Excitation properties and emission spectra for Mod 3 were calculated with the parallel version of the TD-OT- $\omega\text{B97X-D3}$  method on the basis of the OT- $\omega\text{B97XD}$  ( $\omega = 0.0984 \text{ Bohr}^{-1}$ ) optimized  $T_1$  structures using version 4.1 of the ORCA package [33]. We opted for the all electron



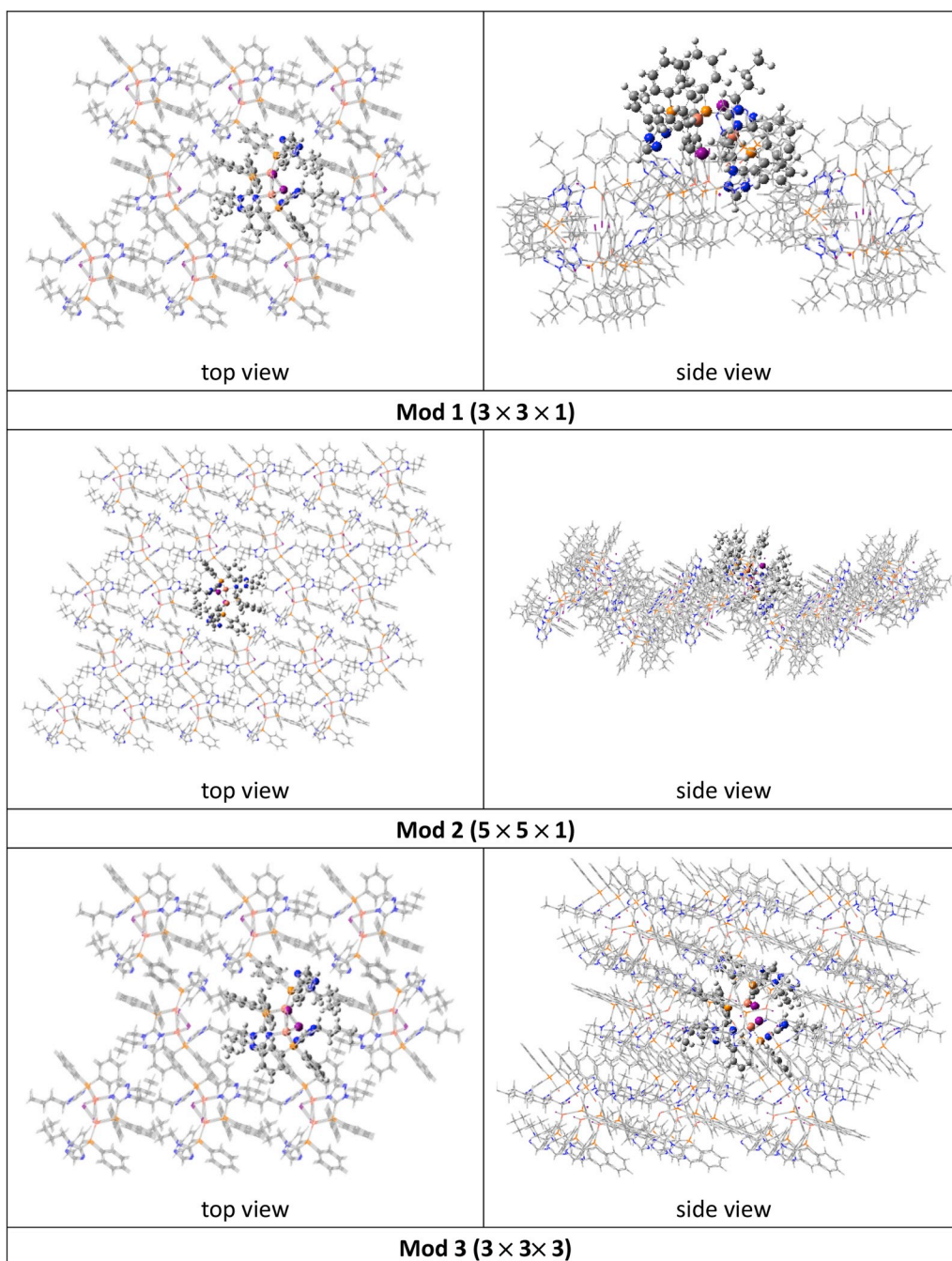


**Fig. 3.** Diagram of constructing the ONIOM QM/MM model for the  $\text{Cu}_2\text{I}_2(\text{P}^*\text{N})_3$  crystal. All constructed models are two-level ONIOM, the centered  $\text{Cu}_2\text{I}_2(\text{P}^*\text{N})_3$  is treated as high layer (130 atoms) with QM mechanism; remaining molecules are regarded as low layer at the MM level. Mod 1: 2-dimensional model ( $3 \times 3 \times 1$ ), low layer of 1040 atoms; Mod 2: 2-dimensional model ( $5 \times 5 \times 1$ ), low layer of 3120 atoms; Mod 3: 3-dimensional model ( $3 \times 3 \times 3$ ), low layer of 3380 atoms.

scalar relativistically recontracted DKH-def2-TZVP(-f) basis set discarding all f-functions of higher angular momentum for the Cu, P, N, C, and H atoms [34], while the old-DKH-TZVP basis set was employed for iodine in conjunction with the corresponding SARC/J auxiliary basis set required for the RIJCOSX algorithm in order to speed up the calculations [35]. Scalar relativistic effects were treated using the second order Douglas-Kroll-Hess (DKH) method. The SOC effects along with the ZFS interactions are the SOC quasi-degenerate perturbation theory (QDPT) approach [36], where we employed an accurate multicenter spin-orbit mean-field (SOMF) of the Breit-Pauli SOC operator on all centers [37]. This operator explicitly deals with the spin-same-orbit and spin-other-orbit terms in its two-electron part, and leads to a mixing of different multiplicities ( $\Delta S = 0, \pm 1$ ).

#### 2.4. Radiative and nonradiative rate constants

Under the Frank-Condon approximation, based on the Fermi's golden theory, the radiative rate constants, called as fluorescence rate  $k_r(S)$ , and phosphorescence rate  $k_r(T)$ , are obtained by the integration of the whole emission spectrum  $\sigma_{em}(\omega, T)$  at different temperatures, which can be expressed as the following equations (3) and (4) [25,38]:

$$\sigma_{em}(\omega, T) = \frac{2\omega^3}{3\pi c^3 \hbar^4} |\mu(S_0 \leftarrow T_1/S_1)| \int e^{-i\omega t} e^{i\omega S_0 - T_1/S_1} Z_i^{-1} \rho_{em}(t, T) dt \quad (3)$$

$$k_r = \int_0^\infty \sigma_{em}(\omega, T) d\omega \quad (4)$$

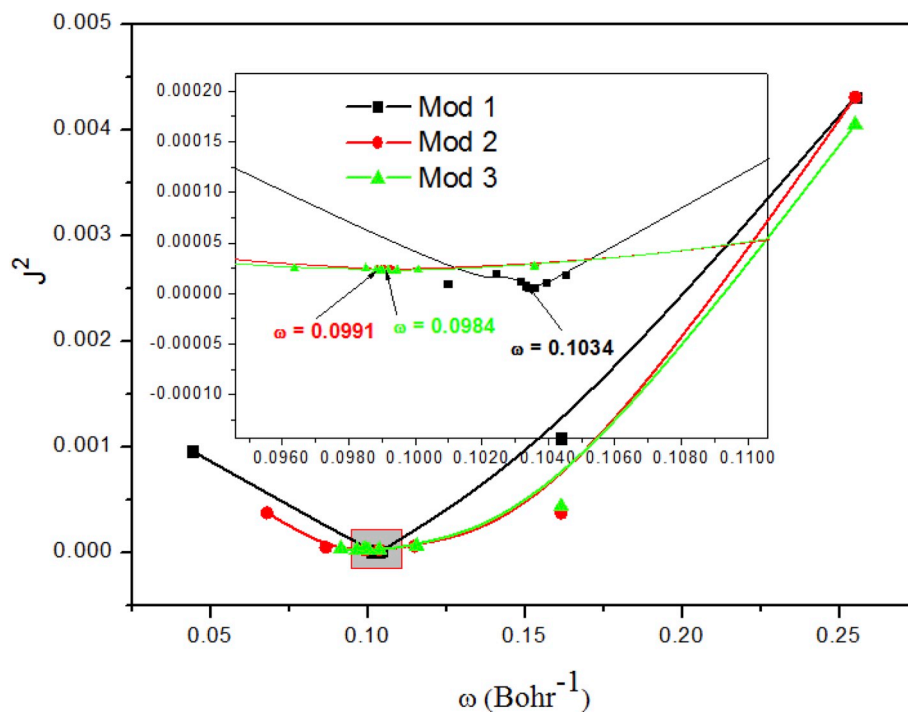


**Fig. 4.**  $J^2$  as a function of the optimally tuned range-separation parameter  $\omega$  ( $\text{bohr}^{-1}$ ) based on equation (2) of  $\omega$ B97XD (the default value of  $\omega = 0.2$ ) functional for Mod 1, Mod 2, and Mod 3. The minimum displays the optimal value of  $\omega$ .

here,  $\mu$  is the electric transition dipole moment between two electronic state; and the  $\rho_{\text{em}}(t, T) = \text{Tr}[e^{i\tau\hat{H}_{T_1/S_1}} e^{i\tau\hat{H}_{S_0}}]$  is the TVCF formula which can be solved analytically by multidimensional Gaussian integrations;  $Z_{T_1}^{-1} = \sum_{v=\{0_1, 0_2, \dots, 0_N\}} e^{-\beta E_v^{T_1}}$  expresses the partition function, here  $N$  is the number of normal modes. In addition, at ambient temperature limit, the radiative decay rates can be calculated by Einstein spontaneous emission rate equation (5) [39,40].

$$k_{r,\zeta} = \frac{4e^2}{3c^3\hbar^4} \Delta E_{S_0 \leftarrow T_{1,\zeta}}^3 |\mu(S_0 \leftarrow T_{1,\zeta})|^2 \quad (5)$$

wherein  $\Delta E_{S_0 \leftarrow T_{1,\zeta}}$  indicates a vertical emission energy, and subscript  $\zeta$  denotes the substates of triplet state  $T_1$ .

Using first-order perturbation theory, the nonradiative internal conversion rate  $k_{\text{nr}}$  between two electronic states with the same spin states can be written as the following equation

$$k_{\text{nr}} = \frac{1}{\hbar^2} R_{kl} \int_{-\infty}^{\infty} dt e^{i\omega_{S_1, S_0} t} \rho_{S_1, S_0}(t, T) \quad (6)$$

In which place,  $R_{kl} = \langle \Phi_{S_0} | \hat{P}_{S_1, k} | \Phi_{S_1} \rangle \langle \Phi_{S_1} | \hat{P}_{S_1, l} | \Phi_{S_0} \rangle$  is the nonadiabatic electronic coupling matrix between two electronic states; and  $\hat{P}_{S_1, k} = -i\hbar \partial / \partial Q_{S_1, k}$  represents the normal momentum operator of the  $k$ th mode in the  $S_0$  state.

Rate constants for nonradiative ISC from initial  $S_1$  state to the final  $T_1$  state could be estimated as follows [25,41]:

$$k_{\text{ISC}} = \frac{2\pi}{\hbar} |\langle T_1 | \hat{H}_{\text{SOC}} | S_1 \rangle|^2 Z_{T_1}^{-1} \sum_{v,u} e^{-\beta E_v^{T_1}} |\langle \Theta_{T_1, v} | \Theta_{S_1, u} \rangle|^2 \delta(E_{T_1, v} - E_{S_1, u}) \quad (7)$$

By means of the Fourier transform for the  $\delta$  function, equation (7) can be rewritten as equation (8).

$$k_{\text{ISC}} = \frac{1}{\hbar^2} |\langle T_1 | \hat{H}_{\text{SOC}} | S_1 \rangle|^2 \int_{-\infty}^{\infty} dt \left[ e^{i\omega_{T_1, S_1} t} Z_{T_1}^{-1} \rho_{\text{ISC}}(t, T) \right] \quad (8)$$

wherein  $|\langle T_1 | \hat{H}_{\text{SOC}} | S_1 \rangle|$  is the SOC matrix between  $T_1$  and  $S_1$ ;  $u$  and  $v$  denote the vibrational quantum numbers of the initial  $S_1$  state and the

final  $T_1$  state in equation (7), respectively; while the  $\delta$  function is to keep the conservation of energy.

For the above-mentioned equations, their detailed derivation and solution could be found in Shuai's and Peng's works. All calculations were carried out using the MOMAP 1.0 program promoted by Shuai's teams [25].

### 3. Results and discussion

#### 3.1. Geometric structures of $\text{Cu}_2\text{I}_2(\text{P}^{\text{N}})_3$

The accurate optimization of molecular geometry is a prerequisite for the calculation of photophysical properties. In this work, the key geometrical parameters of the  $S_0$  states of the  $\text{Cu}_2\text{I}_2(\text{P}^{\text{N}})_3$  molecule crystal using different calculation approaches with B3LYP, CAM-B3LYP, PBE, and OT- $\omega$ B97XD for three models are collected in Table 1, together with the X-ray crystal structure for comparison. It is obvious from Table 1 that the OT- $\omega$ B97XD method is in excellent agreement with the X-ray crystal data [20]. This means that adopted OT- $\omega$ B97XD method is suitable for this complex. The optimally tuned  $\omega$  values calculated by the tuning optDFTw procedure for Mod 1, Mod 2, and Mod 3 in the ONIOM framework are illustrated in Fig. 4 [31]. It can be seen from Fig. 4 that the optimal  $\omega$  values substantially reduced to 0.0984, 0.0991, and 0.1034  $\text{Bohr}^{-1}$  for Mod 3, Mod 2, and Mod 1, respectively, as compared to the default value of  $\omega = 0.2 \text{ Bohr}^{-1}$  of the  $\omega$ B97XD functional. According to the range-separated density functional theory, the tuning  $\omega$  value of a specific system can reflect the overall delocalization degree of the electrons, that is, the inverse relationship between the tuning  $\omega$  value and the extent of electron delocalization. The three models have different electron delocalization due to the different  $\omega$  values, wherein the  $\omega$  value of Mod 3 is the minimum ( $\omega = 0.0984 \text{ Bohr}^{-1}$ ) and the delocalization degree of electron density is the maximum, which indicates that there is a few long-range interaction from exact HF exchange integral. These results further indicate that it is vital important to accurately set up the different ONIOM models for the solid states because of having a great impact on the electronic description for the

**Table 1**

Comparison of optimized vital structural parameters with bond Distances (Å) and angles (deg) at equilibrium geometries of the ground states for  $\text{Cu}_2\text{I}_2(\text{P}^*\text{N})_3$  in the ONIOM level with those of experimental crystal parameters.

	B3LYP			CAM-B3LYP			OT- $\omega$ B97XD			PBE	Exp. value
	Mod 1	Mod 2	Mod 3	Mod 1	Mod 2	Mod 3	Mod 1	Mod 2	Mod 3		
R(Cu1–Cu2)	3.1978	3.2001	3.1083	3.1437	3.1457	3.0738	3.0967	3.1203	<b>3.0405</b>	2.8297	<b>2.8405</b>
R(Cu1–I1)	2.9047	2.9025	2.9156	2.8595	2.8603	2.8698	2.8743	2.8783	<b>2.8831</b>	2.6726	<b>2.6566</b>
R(Cu1–I2)	2.8051	2.8068	2.7691	2.7604	2.7603	2.7341	2.7575	2.7767	<b>2.7346</b>	2.6435	<b>2.6249</b>
R(Cu2–I1)	2.9718	2.9752	2.9109	2.9235	2.9228	2.8793	2.9260	2.9367	<b>2.8951</b>	2.6990	<b>2.6970</b>
R(Cu2–I2)	2.8772	2.8742	2.8916	2.8475	2.8472	2.8588	2.8676	2.8664	<b>2.8699</b>	2.6743	<b>2.6543</b>
R(Cu1–P1)	2.1979	2.1981	2.1888	2.1800	2.1801	2.1745	2.1796	2.1858	<b>2.1780</b>	2.2346	<b>2.2529</b>
R(Cu1–P2)	2.2272	2.2273	2.2253	2.2081	2.2081	2.2089	2.2038	2.2159	<b>2.2080</b>	2.2435	<b>2.2498</b>
R(Cu2–N1)	1.9489	1.9492	1.9511	1.9410	1.9413	1.9439	1.9502	1.9407	<b>1.9538</b>	2.0449	<b>2.0563</b>
R(Cu2–P3)	2.1754	2.1752	2.1729	2.1585	2.1586	2.1576	2.1606	2.1684	<b>2.1594</b>	2.2068	<b>2.2227</b>
$\angle \text{P1Cu1P2}$	118.05	118.06	115.83	116.97	116.98	115.48	115.16	116.57	<b>114.48</b>	111.32	<b>111.74</b>
$\angle \text{N1Cu2P3}$	121.16	121.12	122.71	120.71	120.68	122.19	119.43	120.24	<b>120.85</b>	114.44	<b>114.91</b>
$\angle \text{P1Cu1I1}$	101.59	99.43	102.02	101.86	101.81	102.06	102.01	102.16	<b>102.79</b>	105.44	<b>104.66</b>
$\angle \text{N1Cu2I2}$	113.41	111.36	113.17	113.70	113.06	113.41	114.47	114.33	<b>113.88</b>	112.94	<b>112.65</b>

proportion of DFT-type exchange and HF exact exchange in the exchange functional.

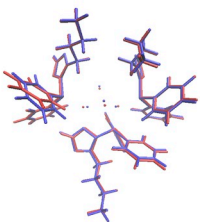
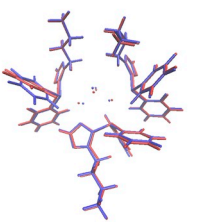
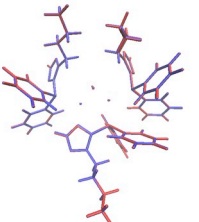
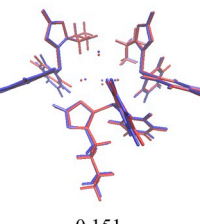
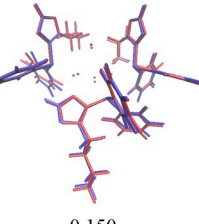
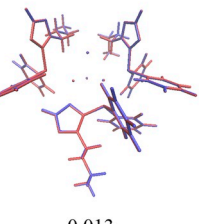
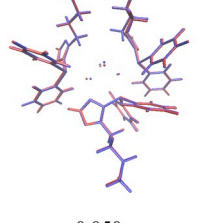
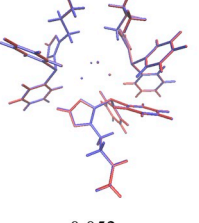
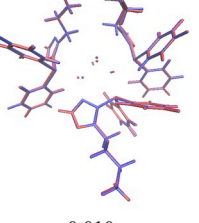
Fig. 2 sketches the dinuclear copper(I) complex of  $\text{Cu}_2\text{I}_2(\text{P}^*\text{N})_3$ , in which two Cu centers are connected by two I-bridges in a  $\text{Cu}_2\text{I}_2$  metal halide core, and additionally by a third bridging  $\text{P}^*\text{N}$  ligand bearing five-membered heterocyclic moiety such as 1, 2, 4-triazole. Analyzing the geometrical parameters in Table 1, at the OT- $\omega$ B97XD level, the corresponding Cu1–I2, Cu2–I1, Cu1–P1, and Cu2–P3 bonds are calculated to be lengths of 2.7575 (2.7767) [2.7346], 2.9260 (2.9367) [2.8951], 2.1796 (2.1858) [2.1780], and 2.1606 (2.1684) [2.1594] Å for Mod 1 (Mod 2) [Mod 3], respectively. In addition, two vital angles of the  $\angle \text{P1–Cu1–I1}$  and  $\angle \text{N1–Cu2–I2}$  are computed to be 102.01° (102.16°)

[102.79°], and 114.47° (114.33°) [113.88°] in Mod 1 (Mod 2) [Mod 3], respectively. The geometrical parameters of Mod 3 at the  $S_0$  state agree well with the crystal X-ray structure, and the largest deviation being less than 1.87° for angles and 0.27 Å for bond lengths.

Based on the Franck-Condon principle and Fermi's golden rule, the geometric deformations between  $S_0$  and  $S_1$  or  $T_1$  can largely control the nonradiative decay rate and the spectral shape. That is also to say, the nonradiative decay rates of  $S_1 \rightarrow S_0$ ,  $T_1 \rightarrow S_0$  and  $T_1 \leftrightarrow S_1$  mainly depend on the geometric deformation between  $S_0$  and  $S_1$ ,  $S_0$  and  $T_1$  as well as  $T_1$  and  $S_1$  of the  $\text{Cu}_2\text{I}_2(\text{P}^*\text{N})_3$  molecule. The geometric changes among  $S_0$ ,  $S_1$  and  $T_1$  are illustrated in Table 2 for providing a visual comparison. Recently, the root of the mean of squared displacement (RMSD) with the

**Table 2**

Comparison of overlapping ONIOM optimized geometries of the  $S_0$ ,  $S_1$ , and  $T_1$  states for Mod 1, Mod 2, and Mod 3. RMSD = root mean square displacement/deviation..

Model	$S_0$ VS $S_1$	$S_0$ VS $T_1$	$S_1$ VS $T_1$
Mod 1			
RMSD <sup>a</sup>	0.160	0.159	0.012
Mod 2			
RMSD	0.151	0.150	0.013
Mod 3			
RMSD	0.050	0.052	0.010

formula as  $\text{RMSD} = \sqrt{1/n \sum_i^{\text{atom}} [(x_i - x'_i)^2 + (y_i - y'_i)^2 + (z_i - z'_i)^2]}$ , is a practical tool to quantitatively characterize the geometric changes, and the values of RMSD between two states are estimated by the Multiwfn program of Tian Lu development [42]. It is found that the geometric changes of  $S_0$  vs  $S_1$  or  $T_1$  in Mod 1 and Mod 2 are more significant than that in Mod 3 with the RMSD values of 0.050 Å and 0.052 Å respectively, as shown in Table 2. Thus, the paths of nonradiative energy consumption are partly forbidden, and the radiation efficiency of fluorescence or phosphorescence is expected to improve in Mod 3. For investigating the ISC and RISC processes, the geometric changes between  $S_1$  and  $T_1$  states are also compared for three models. The values of RMSD are 0.012, 0.013, and 0.010 Å from Mod 1 to Mod 3, respectively, which are much smaller and these show a small variation of the geometries for the  $S_1$  and  $T_1$  states in ISC and RISC processes. Especially for the Mod 3, the non-radiative energy consumption is minimal and enhanced ISC and RISC probabilities, which provides the possibility for the occurrence of TADF.

### 3.2. Properties of excited states of $\text{Cu}_2\text{I}_2(\text{P}^*\text{N})_3$

The electronic energies, adiabatic energy differences, and vertical emission energies of  $\text{Cu}_2\text{I}_2(\text{P}^*\text{N})_3$ , for difference model environment were calculated by employing the TD-OT- $\omega$ B97XD and TD-CAM-B3LYP functionals (see Table 3). Besides, emission spectra were also simulated by performing vertical  $S_1 \rightarrow S_0$  and  $T_1 \rightarrow S_0$  transitions at the scalar relativistic DKH TD-OT- $\omega$ B97XD level with and without SOC effects by means of QDPT from the optimized  $T_1$  structure for Mod 3, as plotted in Fig. 5. The lowest excited state of experimental emission spectrum without the SOC interactions demonstrates that there is a weak band at 420 nm (2.95 eV), which belongs to the vertical transition of  $S_1 \rightarrow S_0$  [19]. From Fig. 5, the calculated and the experimental spectrums are seen to completely match, with the simulated value of 423 nm. The calculated frontier orbitals show that the HOMO is mainly originated from a linear combination of the d-orbitals of the Cu(I) atoms (32%) with the p-orbitals of the iodide atoms (41%), in other words, located mainly on the Cu(I)-I core, whereas the LUMO is mainly distributed over the bridging of 1N-n-butyl-5-diphenyl-phosphino -1,2,4-triazole (see Fig. 6). It reveals that a transition from the spatially well separated HOMO to LUMO should be assigned as (copper + iodide)-to-ligand (M + I) LCT transition, shortly called as MLCT. The  $^1\text{MLCT}$   $S_1$  excited state is mainly single excitation with both of 98% of HOMO  $\rightarrow$  LUMO character at the optimized  $S_1$  and  $T_1$  geometries, this means that HOMO and LUMO are approximately equivalent to “hole” and “electron” of transition state.

In addition, the partial and total densities of states were carried out by VASP package without structure relaxation for the  $\text{Cu}_2\text{I}_2(\text{P}^*\text{N})_3$  crystal, as shown in Fig. 7. And Fig. 7 shows that the lowest energy excited state formed at the  $\text{Cu}_2\text{I}_2(\text{P}^*\text{N})_3$  crystal is a charge transfer state with the electron localized on the bridging of  $\text{P}^*\text{N}$  LUMO and the hole located on the Cu + I HOMO. Photoexcitation of copper + iodide leads to electron transfer onto the bridging ligand of  $\text{P}^*\text{N}$ , while photoexcitation

of the bridging ligand of  $\text{P}^*\text{N}$  results in hole transfer to the copper + iodide core. The charge densities of the HOMO and LUMO orbitals are shown in Fig. 7c. In general, the more significant is the delocalization between donor and acceptor, the stronger is the interaction. The donor state for the hole transfer is localized strongly on the copper + iodide core, indicating weakened donor-acceptor coupling. These results are consistent with those of quantum chemistry.

Upon the spectra including SOC, it can be seen from Fig. 5 that the shape of the spectrum does not change significantly. For example, the  $S_1 \rightarrow S_0$  emission spectrum at 425 nm ( $23554 \text{ cm}^{-1}$ ) shows slightly red-shifted compared with that of without SOC, and it basically retains  $S_1 \rightarrow S_0$  (M + I) LCT features. As to the  $T_1 \rightarrow S_0$  emission, it is theoretically forbidden under a non-relativistic treatment, however, relativistic SOC effects can couple these forbidden transitions, leading to nonzero transition probability. Thus, the formally spin forbidden  $T_1 \rightarrow S_0$  excitation is activated via SOC interaction. The  $T_1 \rightarrow S_0$  excitation, at 448 nm gains small oscillator strength ( $f \approx 6.534 \times 10^{-5}$ ) for Mod 3 at the TD- $\omega$ B97XD3/DKH-def2-TZVP(-f) level (see Fig. 5 green line). Fig. 6 shows that the  $T_1$  state is also mainly single excitation with both of 99% of HOMO  $\rightarrow$  LUMO character at the  $S_1$  and  $T_1$  geometries, having the same character of (Cu + I)-to-ligand (M + I) LCT transition with the  $S_1$  state. This implies that the  $S_1$  and  $T_1$  states have the same orbital configurations.

According to the above discussion, the  $S_1$  and  $T_1$  states have the same orbital configurations,  $^1\text{MLCT}$  and  $^3\text{MLCT}$  from the single HOMO  $\rightarrow$  LUMO excitations. We know that a key requirement of the TADF occurrence is very small singlet-triplet splitting energy,  $\Delta E(S_1-T_1)$  between the  $S_1$  and  $T_1$  excited states under the help of thermal energy. Whereas, in this situation,  $\Delta E(S_1-T_1)$  is well approximated by the exchange integral (also namely as twice the exchange coupling constant,  $J_{\text{H,L}}$ ) for HOMO  $\phi_{\text{H}}$  and LUMO  $\phi_{\text{L}}$  as the following equation [10].

$$J_{\text{H,L}} = c_J \iint \phi_{\text{H}}(\vec{r}_1) \phi_{\text{L}}(\vec{r}_2) \frac{1}{|\vec{r}_2 - \vec{r}_1|} \phi_{\text{H}}(\vec{r}_2) \phi_{\text{L}}(\vec{r}_1) d^3r_1 d^3r_2 \\ = c_J \iint \rho_{\text{H,L}}(\vec{r}_1) \frac{1}{|\vec{r}_2 - \vec{r}_1|} \rho_{\text{H,L}}(\vec{r}_2) d^3r_1 d^3r_2 \quad (9)$$

Here,  $c_J = e^2/4\pi\epsilon_0$  is a numerical constant;  $\rho_{\text{H,L}} = \phi_{\text{H}}(\text{r}) \cdot \phi_{\text{L}}(\text{r})$  is called the transition density. From equation (9), the exchange integral can be estimated as the electrostatic interaction of the transition density  $\rho_{\text{H,L}}$  with itself. The estimated transition density is depicted schematically in Fig. 6. The important observation is that the  $S_1 \rightarrow S_0$  and  $T_1 \rightarrow S_0$  excitations have the small transition densities in absolute value in spatial regions, which implies that  $\Delta E(S_1-T_1)$  is small and the spatial overlap of the HOMO and LUMO is also small. This may also be explained by representing the molecular orbitals by linear combinations of orbitals localized in different spatial regions. Besides, we calculated the density differences of the  $S_1 \rightarrow S_0$  and  $T_1 \rightarrow S_0$  excitations by using  $\Delta\rho(\text{r}) = \Delta\rho^{\text{ele}}(\text{r}) - \Delta\rho^{\text{hole}}(\text{r})$ , and plotted them in the bottom of Fig. 6, where significant electron density difference are found between the electron donor of copper + iodide core with the depletion density (coffee color) and the 1N-n-butyl-5-diphenyl-phosphino -1,2,4-triazole ligand acceptor with

**Table 3**

Calculated electronic energies (in a.u.), adiabatic energy differences  $\Delta E$  eV, and vertical emission energies,  $\Delta E_{\text{v}}$  eV for the  $\text{Cu}_2\text{I}_2(\text{P}^*\text{N})_3$  complex in difference model environment with OT- $\omega$ B97XD and CAM-B3LYP functionals.

	OT- $\omega$ B97XD						
	$E(S_0)$	$E(S_1)$	$E(T_1)$	$\Delta E(S_0-S_1)$	$\Delta E(S_1-T_1)$	$\Delta E_{\text{v}}(S_0-S_1)$	$\Delta E_{\text{v}}(S_1-T_1)$
Mod 1	-6913.935282	-6913.849898	-6913.852101	2.323	0.059	2.667	0.132
Mod 2	-6914.311681	-6914.234240	-6914.230637	2.107	-0.098	2.687	0.135
Mod 3	-6913.975026	-6913.885106	-6913.886885	2.447	0.048	2.920	0.155
	CAM-B3LYP						
	$E(S_0)$	$E(S_1)$	$E(T_1)$	$\Delta E(S_0-S_1)$	$\Delta E(S_1-T_1)$	$\Delta E_{\text{v}}(S_0-S_1)$	$\Delta E_{\text{v}}(S_1-T_1)$
Mod 1	-6912.833819	-6912.727257	-6912.700713	2.898	-0.722	2.563	0.134
Mod 2	-6912.833870	-6912.727286	-6912.744878	2.899	0.478	2.545	0.144
Mod 3	-6912.826749	-6912.715207	-6912.732748	3.035	0.477	2.639	0.131



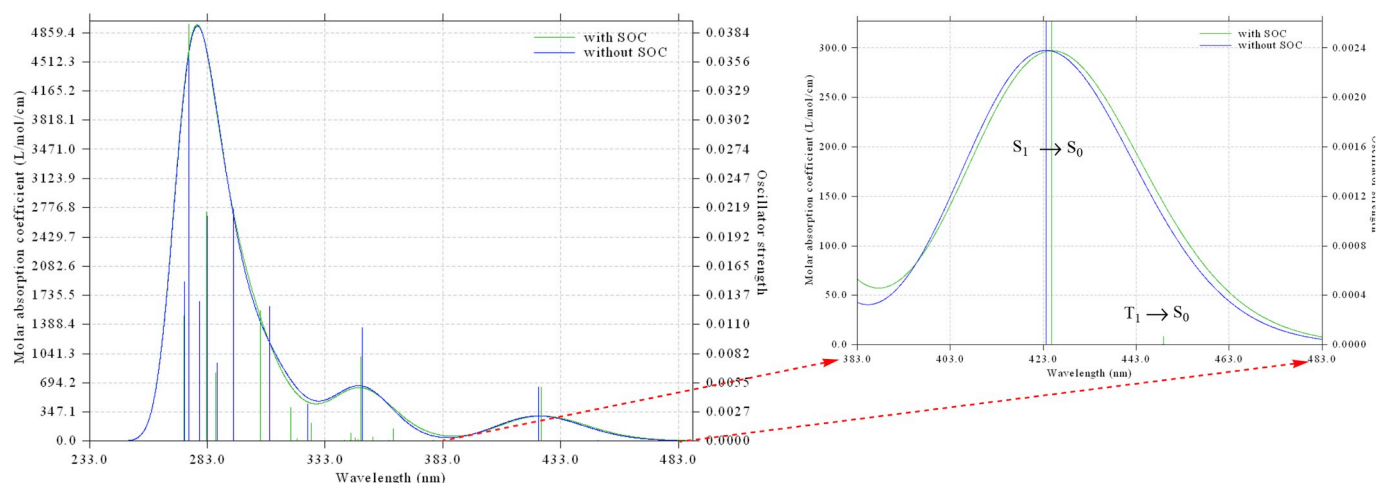


**Fig. 5.** Calculated emission spectra in crystal for Mod 3 by the scalar relativistic Douglas-Kroll-Hess(DKH) Hamiltonian (blue line)- and SOC-based (green line) TD-DFT, employing  $\omega$ B97X-D3 functional and DKH-def2-TZVP(-f) basis set (old-DKH-TZVP for the I atom) at the  $T_1$  geometry. Experimental value of the  $S_1 \rightarrow S_0$  transition energy is 2.95 eV (420.3 nm) from ref. 19. (For interpretation of the references to color in this figure legend, the reader is referred to the Web version of this article.)

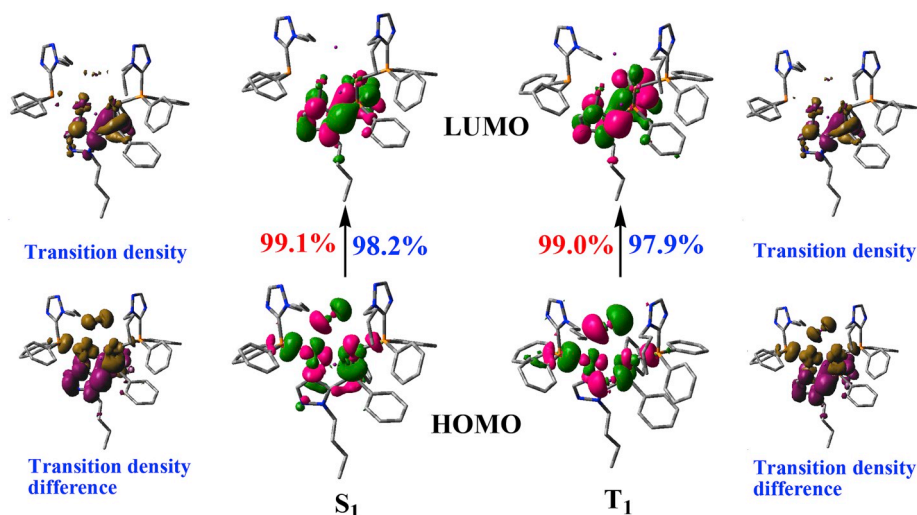


**Fig. 6.** Frontier orbitals (HOMO and LUMO) of  $\text{Cu}_2\text{I}_2(\text{P}^*\text{N})_3$ , transition density difference of HOMO  $\rightarrow$  LUMO and proportion of HOMO  $\rightarrow$  LUMO for the  $S_1$  (blue) and  $T_1$  (red) states of the optimized  $S_1$  and  $T_1$  geometries. (For interpretation of the references to color in this figure legend, the reader is referred to the Web version of this article.)

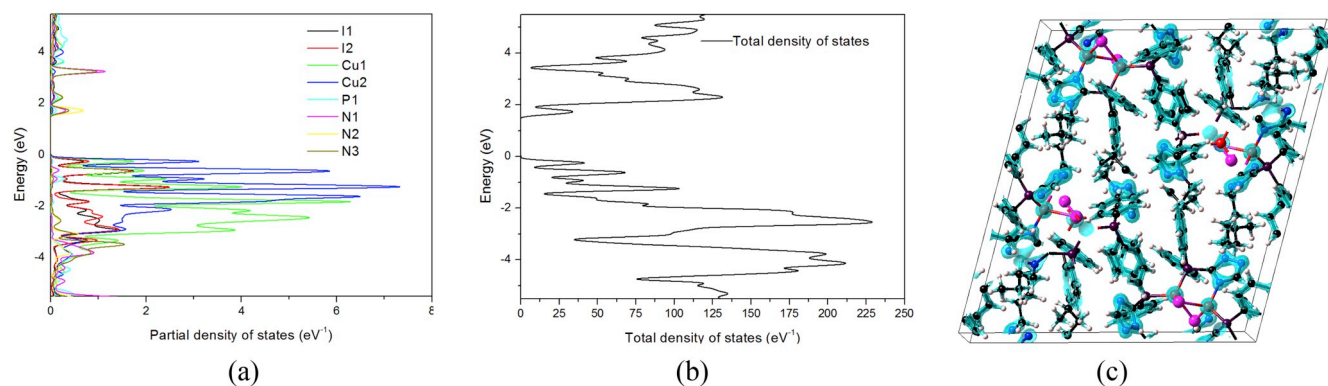


**Fig. 7.** Calculated partial density of states (a), total density of states (b), band structure (c), and distribution of total valence charge density of the optimized  $\text{Cu}_2\text{I}_2(\text{P}^*\text{N})_3$  crystal cell with PBE exchange-correlation functional within a generalized gradient approximation (GGA) and the projector augmented-wave (PAW) potential.



the excess density (purplish red). This indicates that the hole and electron on the  $\text{Cu}_2\text{I}_2(\text{P}^{\text{N}})_3$  molecule are completely separated, and this larger separated distance is defined having a CT excited nature, which leads to selecting the OT- $\omega\text{B97XD}$  and CAM-B3LYP approaches to evaluate  $\Delta E(\text{S}_1\text{-T}_1)$  for three models (see Table 3). Compared to the experimental value of  $\Delta E(\text{S}_1\text{-T}_1) = 430 \text{ cm}^{-1}$ , it is apparent that OT- $\omega\text{B97XD}$  gives the best prediction of  $\Delta E(\text{S}_1\text{-T}_1)$ , adiabatic energy difference,  $\Delta E(\text{S}_1\text{-T}_1)$  of Mod 3 is  $0.048 \text{ eV}$  ( $\approx 387 \text{ cm}^{-1}$ ), matching the experimental value of  $430 \text{ cm}^{-1}$  very well [19].

### 3.3. Radiative rate constants of $\text{Cu}_2\text{I}_2(\text{P}^{\text{N}})_3$

In this section, the simple Einstein spontaneous emission formula of equation (5) is used to estimate fluorescence  $k_r(\text{S})$  and phosphorescence  $k_r(\text{T})$  rate constants, these data are summarized in Table 4. As we know, a detailed study of photophysical properties of the emitting  $\text{T}_1$  state is vital for the excited state dynamics understanding in TADF material. For the phosphorescence  $k_r(\text{T})$ , actually, the direct electric transition dipole moment of the  $\text{T}_1 \rightarrow \text{S}_0$  emission is strictly spin-forbidden in an unrelativistic regime. However, for transition metal complexes, the relativistic SOC interactions will split an emitting  $\text{T}_1$  state into three substates ( $\text{T}_{1, \text{I}}$ ,  $\text{T}_{1, \text{II}}$ , and  $\text{T}_{1, \text{III}}$ ) in the zero field, which can cause these substates to have quite different radiative properties. The calculated results reveal a very large energy splitting of the emitting  $\text{T}_1$  state into substates for three models of  $\text{Cu}_2\text{I}_2(\text{P}^{\text{N}})_3$ , for example Mod 3, amounting to  $\Delta E(\text{T}_{1, \text{III}}\text{-T}_{1, \text{I}}) = 17 \text{ cm}^{-1}$ , and  $\Delta E(\text{T}_{1, \text{II}}\text{-T}_{1, \text{I}}) = 10 \text{ cm}^{-1}$ , corresponds to an emitting triplet state which is largely of MLCT character. TD-DFT calculations also support this assignment. These results further indicate that the substates of the emitting  $\text{T}_1$  state do not represent pure triplet state, and they also contain contributions from singlets due to SOC. Thus

**Table 4**

Computed vertical transition energies  $\Delta E$ , oscillator strength  $f$ , radiative rates  $k_r$ , and lifetimes  $\tau$  of the spin sublevels at the  $\text{T}_1$  minimum and the corresponding experimental values in parentheses.

State	$\Delta E$ ( $\text{cm}^{-1}$ )	$f$	$k_r$ ( $\text{s}^{-1}$ )	$\tau$ ( $\mu\text{s}$ )
Mod 1				
$\text{T}_{1, \text{I}}$	20435.2	$1.272 \times 10^{-5}$	$3.543 \times 10^3$	282
$\text{T}_{1, \text{II}}$	20443.2	$2.258 \times 10^{-5}$	$6.295 \times 10^3$	159
$\text{T}_{1, \text{III}}$	20451.1	$1.301 \times 10^{-5}$	$3.630 \times 10^3$	275
Average			$k_r(\text{S}) = 4.489 \times 10^3$	$\tau_{\text{av}}(\text{T}_1) = 223$
$\text{S}_1$	21515.6	$4.873 \times 10^{-3}$	$k_r(\text{T}) = 1.505 \times 10^6$	$\tau(\text{S}_1) = 0.664$
Mod 2				
$\text{T}_{1, \text{I}}$	20570.8	$9.466 \times 10^{-6}$	$2.672 \times 10^3$	374
$\text{T}_{1, \text{II}}$	20579.7	$2.201 \times 10^{-5}$	$6.218 \times 10^3$	161
$\text{T}_{1, \text{III}}$	20587.8	$1.347 \times 10^{-5}$	$3.808 \times 10^3$	263
Average			$k_r(\text{T}) = 4.232 \times 10^3$	$\tau_{\text{av}}(\text{T}_1) = 236$
$\text{S}_1$	21678.1	$5.109 \times 10^{-3}$	$k_r(\text{S}) = 1.601 \times 10^6$	$\tau(\text{S}_1) = 0.625$
Mod 3				
$\text{T}_{1, \text{I}}$	22285.1	$6.538 \times 10^{-6}$	$2.166 \times 10^3$	462
$\text{T}_{1, \text{II}}$	22295.3	$6.534 \times 10^{-5}$	$2.167 \times 10^4$	46 (20) <sup>a</sup>
$\text{T}_{1, \text{III}}$	22302.4	$5.392 \times 10^{-6}$	$1.789 \times 10^3$	559
Average			$k_r(\text{T}) = 8.542 \times 10^3$	$\tau_{\text{av}}(\text{T}_1) = 117$ (55) <sup>a</sup>
$\text{S}_1$	23554.0	$5.038 \times 10^{-3}$	$k_r(\text{S}) = 1.865 \times 10^6$	$\tau(\text{S}_1) = 0.536$ (0.300) <sup>a</sup>

<sup>a</sup> Ref.19.

the discussion of efficient SOC becomes very important.

In order to understand coupling caused by SOC interaction, important coupling states marked using the same colors (blue and pink) are displayed in Fig. 8. The shift in the substate energy mainly originates from a singlet-triplet ( $E_{\zeta}^{\text{ST}}$ ) SOC, which is expressed as equation (10) [43].

$$E_{\zeta}^{\text{ST}} = \sum_n \frac{|\langle \text{T}_{1, \zeta} | \hat{H}_{\text{SOC}} | \text{S}_n \rangle|^2}{E(\text{S}_n) - E(\text{T}_{1, \zeta})}, \zeta = \text{I, II, III} \quad (10)$$

Based on equation (10), the contribution of the SOC from  $\text{S}_1$  for the emitting  $\text{T}_1$  state is almost zero because the  $\text{S}_1$  and  $\text{T}_1$  states have the same configurations,  $1,^3\phi_3\phi_4$ , which violates the principle of conservation of total angular momentum. These analysis is very consistent with the small SOC values calculated ( $\langle \text{T}_{1, \text{I}} | \hat{H}_{\text{SOC}} | \text{S}_1, 0 \rangle = -0.95 i \text{ cm}^{-1}$ ;  $\langle \text{T}_{1, \text{II}} | \hat{H}_{\text{SOC}} | \text{S}_1, 0 \rangle = 8.00 - 2.52 i \text{ cm}^{-1}$ ; and  $\langle \text{T}_{1, \text{III}} | \hat{H}_{\text{SOC}} | \text{S}_1, 0 \rangle = 8.00 + 2.52 i \text{ cm}^{-1}$ ), see Table 5, which would be negligible. One can note in Table 5 that the SOC interactions between the other higher excited states  $\text{S}_n$  ( $n = 2$ , and 3) and  $\text{T}_1$  are very strong. As a case of strong SOC, the SOC values between  $\text{T}_1$  and  $\text{S}_2$  are respectively  $\langle \text{T}_{1, \text{I}} | \hat{H}_{\text{SOC}} | \text{S}_2, 0 \rangle = 6.35 i \text{ cm}^{-1}$ ;  $\langle \text{T}_{1, \text{II}} | \hat{H}_{\text{SOC}} | \text{S}_2, 0 \rangle = 43.86 + 1.37 i \text{ cm}^{-1}$ ;  $\langle \text{T}_{1, \text{III}} | \hat{H}_{\text{SOC}} | \text{S}_2, 0 \rangle = 43.86 - 1.37 i \text{ cm}^{-1}$ , corresponding to three component values of  $H_{\text{SOC}}(x) = -1.93 \text{ cm}^{-1}$ ,  $H_{\text{SOC}}(y) = -62.03 \text{ cm}^{-1}$ , and  $H_{\text{SOC}}(z) = 6.35 \text{ cm}^{-1}$ . It is easily seen from Fig. 8 that the two states are related by moving an electron with spin-flip between the  $\phi_2$  and  $\phi_3$  orbitals (marked by circles). Since both the  $\phi_2$  and  $\phi_3$  orbitals are situated at the copper + iodide core, coming from the d orbitals of Cu and the p orbitals of iodide atoms, their SOC and hence, that of MLCT state, is very strong according to the same center and heavy atom effects. The strong coupling of the  $\text{S}_2$  state and  $\text{T}_1$  state, and the reason is similar to the description of the  $\text{S}_2$  and  $\text{T}_1$  states. Although the other higher excited states also have strong SOC effect, the contributions on ZFS are neglected due to larger energy denominators. As discussed above, a strong SOC induced strong ZFS and strong radiative rates are obtained.

Considering ZFS for the Mod 3, one find that the phosphorescence radiative rates of the three substates are  $k_r, \text{I} = 2.166 \times 10^3 \text{ s}^{-1}$  ( $\tau_{\text{I}} = 462 \mu\text{s}$ ),  $k_r, \text{II} = 2.167 \times 10^4 \text{ s}^{-1}$  ( $\tau_{\text{II}} = 46 \mu\text{s}$ ), and  $k_r, \text{III} = 1.789 \times 10^3 \text{ s}^{-1}$  ( $\tau_{\text{III}} = 559 \mu\text{s}$ ), respectively, in reasonable agreement with experimentally measured values of  $k_r, \text{I} + k_r, \text{III} = 4.4 \times 10^3 \text{ s}^{-1}$  and  $k_r, \text{II} = 5 \times 10^4 \text{ s}^{-1}$ .<sup>14</sup> An averaged emission decay time  $\tau_{\text{av}}$  of three substates can be calculated by the three individual decay times in the light of  $\tau_{\text{av}} = 3(\tau_{\text{I}}^{-1} + \tau_{\text{II}}^{-1} + \tau_{\text{III}}^{-1})^{-1}$  ( $\tau_{\text{I}}$ ,  $\tau_{\text{II}}$ , and  $\tau_{\text{III}}$  denote the emission decay times of the  $\text{T}_{1, \text{I}}$ ,  $\text{T}_{1, \text{II}}$ , and  $\text{T}_{1, \text{III}}$  substates).<sup>43</sup> From Table 4, the average value calculated for the three phosphorescence rate is  $k_r(\text{T}) = 8.542 \times 10^3 \text{ s}^{-1}$  ( $\tau_{\text{av}}(\text{T}_1) = 117 \mu\text{s}$ ), and the rate of the fluorescence is  $k_r(\text{S}) = 1.865 \times 10^6 \text{ s}^{-1}$  ( $\tau(\text{S}_1) = 0.536$ ), which are in good agreement with experimentally measured values of  $\tau_{\text{av}} = 55 \mu\text{s}$  and  $\tau(\text{S}_1) = 0.3 \mu\text{s}$ .<sup>14</sup>

The rate constants with  $k_r(\text{S})$ , and  $k_r(\text{T})$  are also calculated at 77 K and 300 K by using the TVCF method considering the displacement, distortion, and Duschinsky rotation effects, as shown in Table 6. The  $k_r(\text{T})$  values are estimated to be  $4.12 \times 10^3 \text{ s}^{-1}$  and  $3.71 \times 10^3 \text{ s}^{-1}$  for Mod 3, respectively, at 77 K and 300 K, perfectly matching the experimental value ( $= 4.412 \times 10^3 \text{ s}^{-1}$ ) [19]. In contrast, fluorescence rate  $k_r(\text{S})$  is about one order of magnitude of smaller than that of the experimental measures, which is mainly due to the vibration deformation effect leading to the stronger nonradiative transition.

### 3.4. TADF and phosphorescence mechanisms of $\text{Cu}_2\text{I}_2(\text{P}^{\text{N}})_3$

In principle, the small energy splitting  $\Delta E(\text{S}_1\text{-T}_1) = 387 \text{ cm}^{-1}$  between the  $\text{S}_1$  and  $\text{T}_1$  would be well suited for an efficient TADF effect. Hence, TADF is expected to occur. However, for the actual effective occurrence of TADF, the  $\text{S}_1$  state has to be repopulated, which means that the RISC rate  $k_{\text{RISC}}$  from  $\text{T}_1$  to  $\text{S}_1$  should be larger than the rates of radiative and nonradiative decay of  $\text{T}_1$  to  $\text{S}_0$  at ambient temperature. In general, the RISC process should be promoted by the help of SOC

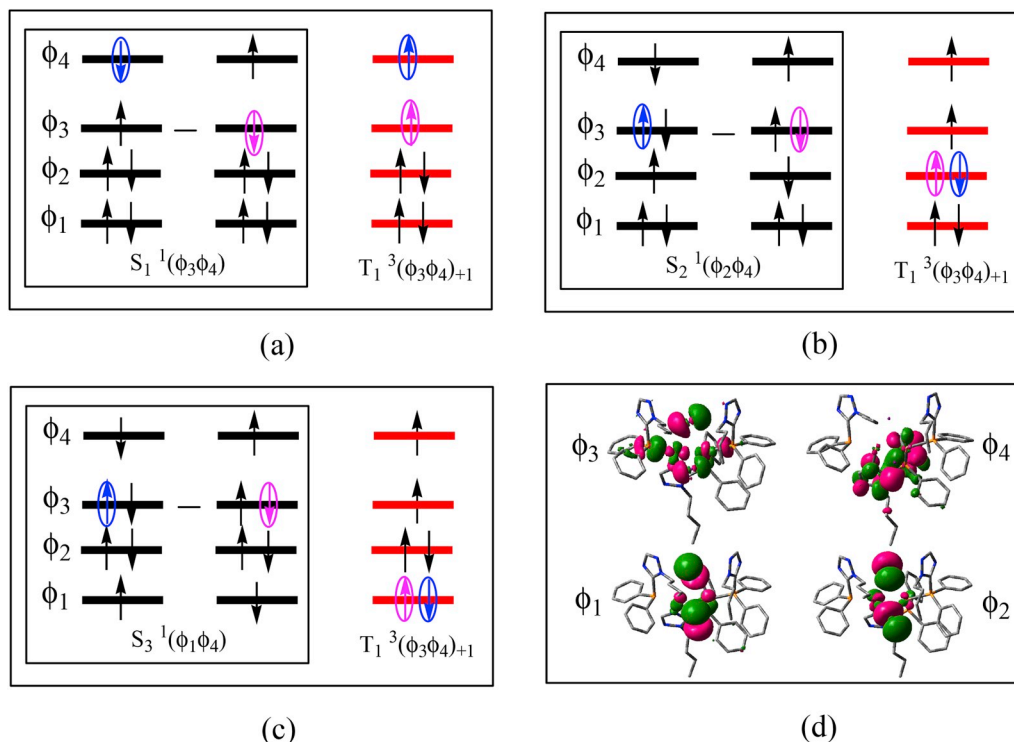


**Fig. 8.** Orbital diagram of the SOC interaction between  $T_1$  and  $S_1$ ,  $S_2$ , and  $S_3$  various states. Electrons on differing orbitals in the coupling states are marked using the same colors (blue and pink). In the schemes (a) case of vanishing SOC are depicted, while (b) and (c) display situations of strong SOC, key active orbitals are plotted in the d part. (For interpretation of the references to color in this figure legend, the reader is referred to the Web version of this article.)

**Table 5**

Calculated SOC matrix elements (in  $\text{cm}^{-1}$ ) between  $T_1$  and  $S_n$  states at the  $T_1$  structure of Mod 3 using the TD- $\omega$ B97X-D3/DKH-def2-TZVP(f)//SARC/J method.

Root		$\langle T_1, 0   H_{\text{SOC}}   S_n, 0 \rangle^a$	$\langle T_1, +1   H_{\text{SOC}}   S_1, 0 \rangle$	$\langle T_1, -1   H_{\text{SOC}}   S_1, 0 \rangle$
$T_1$	$S_0$	0.00, 1.35 <sup>b</sup>	-5.83, -28.74	-5.83, 28.74
$T_1$	$S_1$	0.00, -0.95	8.00, -2.52	8.00, 2.52
$T_1$	$S_2$	0.00, 6.35	43.86, 1.37	43.86, -1.37
$T_1$	$S_3$	0.00, -59.72	69.93, -24.91	69.93, 24.91
$T_1$	$S_4$	0.00, 46.54	33.45, 53.22	33.45, -53.22
$T_1$	$S_5$	0.00, 95.24	-73.47, -0.64	-73.47, 0.64
		$\langle T_1   H_{\text{SOC}}(z)   S_n \rangle$	$\langle T_1   H_{\text{SOC}}(x)   S_n \rangle$	$\langle T_1   H_{\text{SOC}}(y)   S_n \rangle$
$T_1$	$S_0$	1.35	-40.65	8.25
$T_1$	$S_1$	-0.95	3.57	-11.32
$T_1$	$S_2$	6.35	-1.93	-62.03
$T_1$	$S_3$	-59.72	35.23	-98.89
$T_1$	$S_4$	46.54	75.27	-47.30
$T_1$	$S_5$	95.24	-0.91	103.90

<sup>a</sup> Subscript first number indicates different excited states, and second is spin magnetic quantum number; <sup>b</sup> two values mean the real and imaginary parts of the SOC matrix elements.

interaction. As stated in section 3.3, the direct SOC interaction between the  $S_1$  and  $T_1$  states is almost forbidden due to having the same occupied orbitals. Such a situation, the vibronic effects have to be taken into account.

Here, based on equations (7) and (8), the  $k_{\text{ISC}}$  and  $k_{\text{RISC}}$  rates including the vibrational contributions were calculated using the MOMAP program, as summarized in Table 6. For Mod 3, one can find that the RISC rate  $k_{\text{RISC}}$  is  $3.11 \times 10^{10} \text{ s}^{-1}$  at 300 K, which is about 7 order of magnitude larger than the phosphorescence rate  $k_{\text{r}}(T)$ ,  $3.71 \times 10^3 \text{ s}^{-1}$ , and far more than ISC rate  $k_{\text{ISC}}(T_1-S_0)$  of  $6.38 \text{ s}^{-1}$  from the  $T_1$  to  $S_0$  states, which indicates that the  $S_1$  state can be repopulated from the  $T_1$  state by the RISC pathway. The fluorescence rate  $k_{\text{r}}(S) = 2.66 \times 10^5 \text{ s}^{-1}$  seems to be much smaller as compared with the ISC rate of  $1.65 \times$

**Table 6**

Computed luminescence properties of the  $S_1$  and  $T_1$  states at 77 and 300 K by the TVCF method for the crystal models, all units in  $\text{s}^{-1}$ .

Temperature (K)	$k_{\text{r}}(S)$	$k_{\text{nr}}(S)$	$k_{\text{ISC}}$	$k_{\text{RISC}}$	$k_{\text{r}}(T)$	$k_{\text{ISC}}(T_1-S_0)$
Mod 1						
77	$1.39 \times 10^5$	$2.52 \times 10^{11}$	$1.75 \times 10^{11}$	$1.41 \times 10^9$	$5.76 \times 10^2$	$2.54 \times 10^2$
300	$4.43 \times 10^4$	$2.38 \times 10^{11}$	$1.85 \times 10^{11}$	$6.43 \times 10^{10}$	$1.82 \times 10^2$	$2.27 \times 10^2$
Mod 2						
77	$8.01 \times 10^4$	$3.06 \times 10^{11}$	$3.46 \times 10^{10}$	$2.41 \times 10^6$	$3.17 \times 10^2$	$5.05 \times 10^2$
300	$2.40 \times 10^4$	$2.97 \times 10^{11}$	$5.25 \times 10^{10}$	$1.98 \times 10^9$	$9.42 \times 10^1$	$4.78 \times 10^2$
Mod 3						
77	$3.11 \times 10^5$	$2.81 \times 10^8$	$1.17 \times 10^{11}$	$1.73 \times 10^8$	$4.12 \times 10^3$	$2.23 \times 10^8$
300	$2.66 \times 10^5$	$1.63 \times 10^9$	$1.65 \times 10^{11}$	$3.11 \times 10^{10}$	$3.71 \times 10^3$	$6.38 \times 10^0$

$10^{11} \text{ s}^{-1}$ , at the same time, having the larger nonradiative rate  $k_{\text{nr}}(S)$  of  $1.63 \times 10^9 \text{ s}^{-1}$ . It is noteworthy that  $1.65 \times 10^{11} \text{ s}^{-1} \gg 2.66 \times 10^5 \text{ s}^{-1} + 1.63 \times 10^9 \text{ s}^{-1}$ , and  $3.11 \times 10^{10} \gg 3.71 \times 10^3 \text{ s}^{-1} + 6.38 \times 10^0 \text{ s}^{-1}$  are suitable for this  $k_{\text{ISC}} \gg k_{\text{r}}(S) + k_{\text{nr}}(S)$  and  $k_{\text{RISC}} \gg k_{\text{r}}(T) + k_{\text{ISC}}(T_1-S_0)$  conditions based on the kinetic analysis of a three level system proposed by Kirchoff et al. (see Table 6),<sup>39</sup> therefore, populations between the  $S_1$  and  $T_1$  states rapidly equilibrate before decaying radiatively, the delayed fluorescence possibly thus occurs. Fortunately, the emission delayed fluorescence time of  $\tau(\text{TADF}) = 10 \mu\text{s}$  at  $T = 300 \text{ K}$  obtained by fitting equation (1) in Ref. [44] is in excellent agreement with the experimental value of  $8 \mu\text{s}$  (see Fig. 9).

In order to further explore the relationship between vibration and intersystem crossing rate during the conversion processes of  $T_1 \leftrightarrow S_1$ , the Huang-Rhys factor ( $S_i = \omega_i D_i^2 / 2\hbar$ ) and the corresponding reorganization

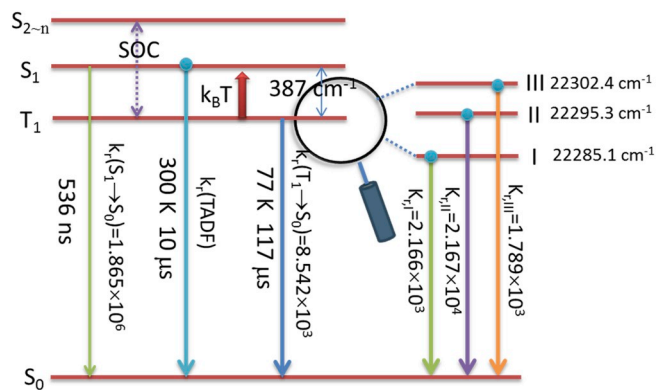


**Fig. 9.** Energy level illustration and decay rates (in  $\text{s}^{-1}$ ) or decay times of the Mod 3. Purpose of  $S_{2-n}$  states displayed is to illustrate an effective SOC pathway. Energy level diagram of the  $T_1$  substates and decay rates (in  $\text{s}^{-1}$ ) are also listed at the right side.

energy ( $\lambda_i = \hbar\omega_i S_i$ ) of vibration mode  $i$  are estimated by the MOMAP program, wherein  $D_i$  is the displacement along the  $i$ th normal mode coordinate between the equilibrium position of two electronic states, and  $\omega_i$  denote the  $i$ th mode frequency, these data are shown in Fig. 10. We know that the extent of geometry relaxation between  $T_1$  and  $S_1$  states

can be measured by the value of Huang-Rhys factor  $S_i$ . Among many vibrations, only parts of vibration modes play an important role in the deformation of geometry inducing the  $T_1 \leftrightarrow S_1$  crossing. As can be seen from Fig. 9 that some low frequency vibration modes ( $<750 \text{ cm}^{-1}$ ) have larger  $S_i$ , such as  $\omega = 187.53 \text{ cm}^{-1}$ ,  $S_i = 0.11$ ;  $\omega = 155.63 \text{ cm}^{-1}$ ,  $S_i = 0.09$ ; as well as  $\omega = 246.30 \text{ cm}^{-1}$ ,  $S_i = 0.06$ , which corresponds to the different distortion vibration of the third bridging P<sup>\*</sup>N ligand bearing five-membered heterocyclic moiety. This implies that the  $T_1 \leftrightarrow S_1$  crossing channel is achieved by the distortion rotation of the third bridging P<sup>\*</sup>N ligand.

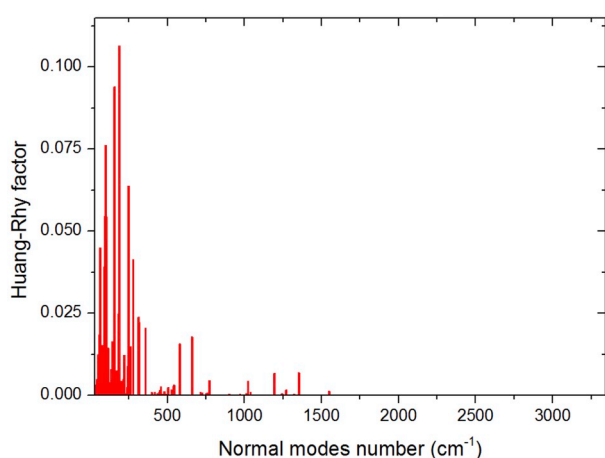
In these favorite “promoting” modes, the Landau-Zener transition probability  $p_{LZ}$  for non-adiabatic transition  $T_1 \rightarrow S_1$  and the electronic transmission coefficient  $k_{el}$  accounting for multiple crossing at the crossing region were also simulated by the following equations [45]:

$$k_{el} = 2p_{LZ}(1 - p_{LZ}) \quad (11)$$

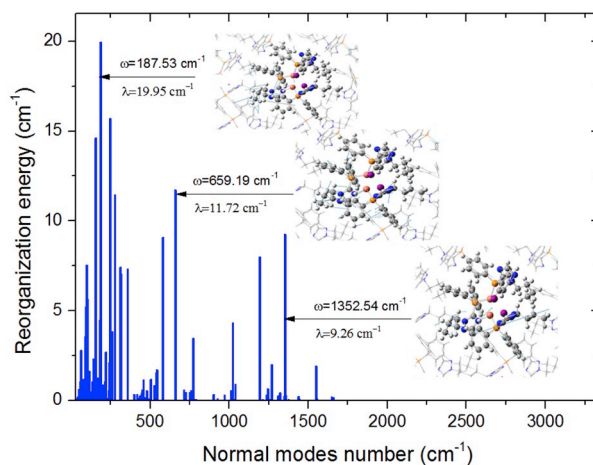
and

$$p_{LZ} = 1 - \exp(-2\pi\gamma), \quad 2\pi\gamma = [\pi^{3/2} |H_{SOC}|^2 / (\hbar\omega_{eff}(\lambda k_B T)^{1/2})]$$

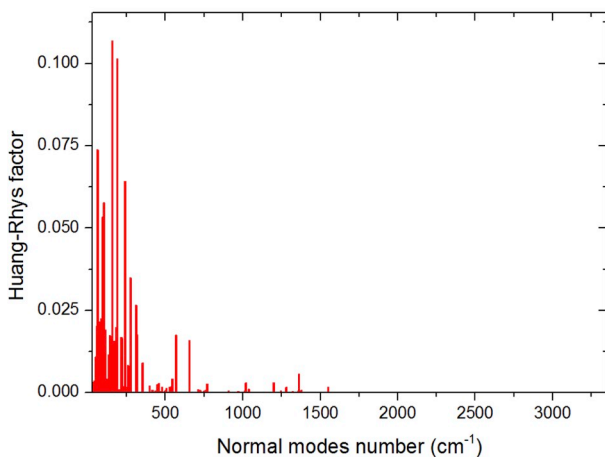
where  $\omega_{eff}$  is the effective frequency along the reaction coordinate, and  $k_B$  the Boltzman constant,  $T$  the temperature. The calculated data are shown in Fig. 11, electronic transmission coefficients  $k_{el}$  from the  $T_1$  to  $S_1$  gradually decrease with increasing temperature, such as  $k_{el} = 23\%$  at 300 K, which will induce us to further analyze the phosphorescence



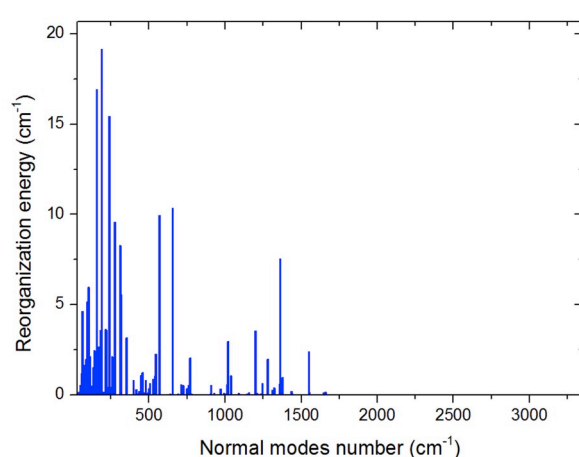
(a)



(b)



(c)



(d)

**Fig. 10.** Calculated Huang-Rhys factors and reorganization energies ( $\text{cm}^{-1}$ ) versus the normal modes on the  $T_1$  (a, b) and  $S_1$  (c, d) potential energy surfaces of Mod 3 in the ISC process, respectively. The largest reorganization energies were inserted into the picture for the  $T_1$  state.

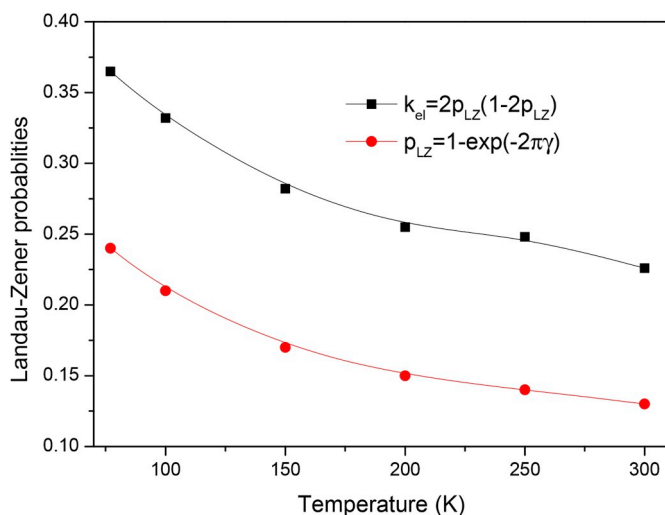


**Fig. 11.** Landau-Zener transition probability,  $p_{LZ}$  and electronic transmission coefficient  $k_{el}$ , from the  $T_1$  state to the  $S_1$  state for Mod 3 as functions of temperature.

radiative.

Through the previous discussion, the  $T_1$  state of the  $Cu_2I_2(P^*N)_3$  complex exhibits distinct admixtures of higher lying singlet states due to stronger SOC, having a larger ZFS, therefore, a relatively fast phosphorescence decay rate of  $k_r(T) = 8.542 \times 10^3$  is obtained. On the other hand, it is characterized by a rigid molecular structure owing to the three-fold bridging the copper centers, leading to lower nonradiative energy dissipation of the excited states, which are supported by the geometrical modification from  $T_1$  to  $S_0$  states, RMSD = 0.052 Å (see Table 2). These would provide the possibility of phosphorescent radiation. In order to visualize the percentage of the intensity originating from the  $S_1$  and from the  $T_1$  state relative to the total intensity in dependence of the temperature. Applying equations (4) and (5) in ref. [44], the calculated intensities of TADF and phosphorescence for Mod 3 are plotted in Fig. 12. At low temperature of <60 K, mainly the  $T_1$  phosphorescence occurs. With increasing temperature, the intensity contributed from the  $T_1$  phosphorescence drastically decreases, while the intensity coming from the  $S_1$  state increases. At 300 K, the emission intensities are stemming by 91% from the  $S_1$  state as TADF and by 9% as phosphorescence from the  $T_1$  state, experimental values as 87% and 13%, respectively, which further shows the ambient temperature emission represents the combined luminescence of phosphorescence and TADF [19].

#### 4. Conclusions

It is essential to deeply explore more about the electronic structures of emitter materials for material improvements and design strategies in the future. In this work, under the premise of accurate optimization for the  $Cu_2I_2(P^*N)_3$  molecule using the optimally tuned range-separated hybrid functional (OT- $\omega$ B97XD) with the ONIOM models, excitation properties and emission spectra of electrons were calculated by applying the TD-OT- $\omega$ B97X-D3 method including scalar relativistic effects, the calculated results perfectly match excellent agreement with experiment values. These indicate that the approach of the optimally tuned range-separated hybrid functional gives an outstanding description for CT excited state properties.

For the geometry optimization, the geometrical parameters of Mod 3 at the  $S_0$  state agree well with the crystal X-ray structure, and the largest deviation being less than  $1.87^\circ$  for angles and  $0.27$  Å for bond lengths. On the basis of a practical tool to quantitatively characterize the geometric changes, also namely as RMSD, the paths of nonradiative energy consumption are partly forbidden from  $S_1$  or  $T_1$  to  $S_0$ , and the radiation

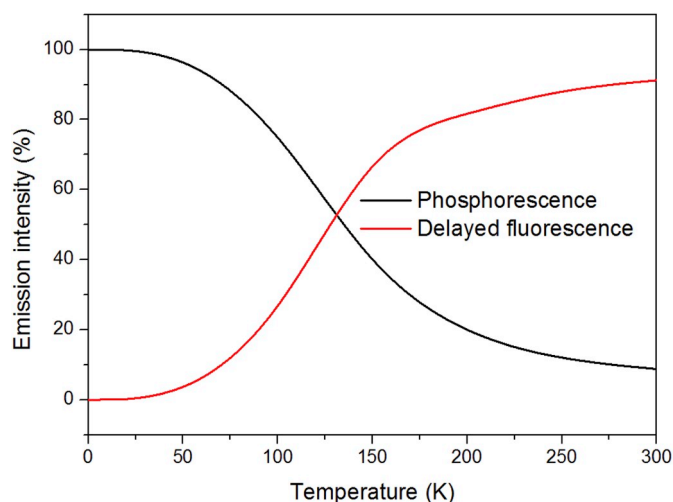


**Fig. 12.** Temperature dependence of the emission intensities coming from the  $S_1$  state (delayed fluorescence) and the  $T_1$  state (phosphorescence). The parameters used are the ones calculated for Mod 3 ( $k_r(S) = 1.865 \times 10^6$ ,  $k_r(T) = 8.542 \times 10^3$ ,  $\Delta E(S_1-T_1) = 387$  cm $^{-1}$ ).

efficiency of fluorescence or phosphorescence is expected to improve. We know that a key requirement of the TADF occurrence is very small singlet-triplet splitting energy,  $\Delta E(S_1-T_1)$  under the help of thermal energy. Compared to the experimental value of  $\Delta E(S_1-T_1) = 430$  cm $^{-1}$ , it is apparent that OT- $\omega$ B97XD gives the best prediction of  $\Delta E(S_1-T_1)$ , adiabatic energy difference,  $\Delta E(S_1-T_1)$  of Mod 3 is 0.048 eV ( $\approx 387$  cm $^{-1}$ ).

The interconversion and decay rates of the  $S_1$  and  $T_1$  states are computed using the TVCF theory at different temperature. one can find that the RISC rate  $k_{RISC}$  is  $3.11 \times 10^{10}$  s $^{-1}$  at 300 K, which is about 7 order of magnitude larger than the phosphorescence rate  $k_r(T)$ ,  $3.71 \times 10^3$  s $^{-1}$ , and far more than ISC rate  $k_{ISC}(T_1-S_0)$  of  $6.38$  s $^{-1}$  from the  $T_1$  to  $S_0$  states, which indicates that the  $S_1$  state can be repopulated from the  $T_1$  state by the RISC pathway. Therefore, the delayed fluorescence possibly thus occurs, and the emission delayed time is  $\tau(\text{TADF}) = 10$   $\mu$ s at  $T = 300$  K (the experimental value of 8  $\mu$ s). In addition, the  $T_1$  state of  $Cu_2I_2(P^*N)_3$  exhibits distinct admixtures of higher lying singlet states due to stronger SOC, having a larger ZFS, therefore, a relatively fast phosphorescence decay rate of  $k_r(T) = 8.542 \times 10^3$  is obtained. At 300 K, the emission intensities are stemming by 91% from the  $S_1$  state as TADF and by 9% as phosphorescence from the  $T_1$  state, experimental values as 87% and 13%, respectively, which further shows the ambient temperature emission represents the combined luminescence of phosphorescence and TADF.

#### Declaration of competing interest

The authors declare that they have no known competing financial interests or personal relationships that could have appeared to influence the work reported in this paper.

#### Acknowledgements

The authors gratefully acknowledge financial support from National Natural Science Foundation of China (Grant No. 21663025, 21663024, 21465021).

#### References

- [1] Y. Tao, K. Yuan, T. Chen, P. Xu, H.H. Li, R.F. Chen, C. Zheng, L. Zhang, W. Huang, *Adv. Mater.* 47 (2014) 7931–7956.
- [2] Z.Y. Yang, Z. Mao, Z.L. Xie, Y. Zhang, S.W. Liu, J. Zhao, J.R. Xu, Z.G. Chi, M. P. Aldred, *Chem. Soc. Rev.* 46 (2017) 915–1016.
- [3] X.-K. Chen, D. Kim, J.-L. Brédas, *Acc. Chem. Res.* 51 (2018) 2215–2224.



- [4] L.-S. Cui, S.-B. Ruan, F. Bencheikh, R. Nagata, L. Zhang, K. Inada, H. Nakanotani, L.-S. Liao, C. Adachi, *Nat. Commun.* 8 (2017), 2250–2249.
- [5] H. Uoyama, K. Goushi, K. Shizu, H. Nomura, C. Adachi, *Nature* 492 (2012) 234–238.
- [6] H. Yersin, A.F. Rausch, R. Czerwieniec, T. Hofbeck, T. Fischer, *Coord. Chem. Rev.* 255 (2011) 2622–2652.
- [7] F. Perrin, *Ann. Phys.* 10 (1929) 169–275.
- [8] M.A. Baldo, D. O'Brien, Y. You, A. Shoustikov, S. Sibley, M. Thompson, S. Forrest, *Nature* 395 (1998) 151–154.
- [9] C. Adachi, M.A. Baldo, M.E. Thompson, S.R. Forrest, *J. Appl. Phys.* 90 (2001) 5048–5505.
- [10] R. Czerwieniec, M.J. Leitl, H.H.H. Homeier, H. Yersin, *Coord. Chem. Rev.* 325 (2016) 2–28.
- [11] J. Föller, M. Kleinschmidt, C.M. Marian, *Inorg. Chem.* 55 (2016) 7506–7516.
- [12] J. Föller, G. Ganter, A. Steffen, C.M. Marian, *Inorg. Chem.* 58 (2019) 5446–5456.
- [13] S.Y. Lin, Q. Peng, Q. Ou, Z.G. Shuai, *Inorg. Chem.* 58 (2019) 14403–14409.
- [14] Y.-J. Gao, W.-K. Chen, Z.-R. Wang, W.-H. Fang, G.-L. Cui, *Phys. Chem. Chem. Phys.* 20 (2018) 24955–24967.
- [15] L.L. Lv, K. Yuan, Y.C. Wang, *Organ. Electron.* 52 (2018) 110–122.
- [16] L.L. Lv, K. Yuan, Y.C. Wang, *Phys. Chem. Chem. Phys.* 20 (2018) 6548–6561.
- [17] L.L. Lv, K. Yuan, Y.C. Zhu, G.F. Zuo, Y.C. Wang, *J. Phys. Chem. A* 123 (2019) 2080–2090.
- [18] H. Yersin, R. Czerwieniec, M.Z. Shafikov, A.F. Suleymanova, *ChemPhysChem* 18 (2017) 3508–3535.
- [19] A. Schinabeck, M.J. Leitl, H. Yersin, *J. Phys. Chem. Lett.* 9 (2018) 2848–2856.
- [20] D.M. Zink, T. Baumann, J. Friedrichs, M. Nieger, S. Bräse, *Inorg. Chem.* 52 (2013) 13509–13520.
- [21] H.T. Sun, C. Zhong, J.-L. Brédas, *J. Chem. Theor. Comput.* 11 (2015) 3851–3858.
- [22] H.T. Sun, Z.B. Hu, C. Zhong, X.K. Chen, Z.R. Sun, J.-L. Brédas, *J. Phys. Chem. Lett.* 8 (2017) 2393–2398.
- [23] T. Körzdörfer, J.L. Brédas, *Acc. Chem. Res.* 47 (2014) 3284–3291.
- [24] L.W. Chung, W.M.C. Sameera, R. Ramozzi, A.J. Page, M. Hatanaka, G.P. Petrova, T. V. Harris, X. Li, Z.F. Ke, F. Liu, H.-B. Li, L. Ding, K. Morokuma, *Chem. Rev.* 115 (2015) 5678–5796.
- [25] Y.L. Niu, W.Q. Li, Q. Peng, H. Geng, Y.P. Yi, L.J. Wang, G.J. Nan, D. Wang, Z. G. Shuai, *MOlecular MATERIALS Property Prediction Package (MOMAP) 1.0: a software package for predicting the luminescent properties and mobility of organic functional materials*, *Mol. Phys.* 116 (2018) 1078–1090.
- [26] A.K. Rappé, C.J. Casewit, K.S. Colwell, W.A. Goddard III, W.M. Skiff, *J. Am. Chem. Soc.* 114 (1992) 10024–10035.
- [27] A.K. Rappé, W.A. Goddard III, *J. Phys. Chem.* 95 (1991) 3358–3363.
- [28] M.J. Frisch, G.W. Trucks, H.B. Schlegel, et al., *Gaussian 09, Revision-D.01*, Gaussian Inc., Wallingford, CT, 2009.
- [29] G. Kresse, J. Furthmüller, *Phys. Rev. B Condens. Matter* 54 (1996) 11169–11186.
- [30] J.P. Perdew, K. Burke, M. Ernzerhof, *Phys. Rev. Lett.* 77 (1996) 3865–3868.
- [31] T. Lu, *optDFTw and scanDFTw Program v1.0*, 2017. .3.8, <http://sobereva.com/346>.
- [32] T. Yanai, D. Tew, N. Handy, *Chem. Phys. Lett.* 393 (2004) 51–57.
- [33] F. Neese, *The ORCA program system, version 4.0*, *WIREs Comput Mol Sci* (2017) e1327, <https://doi.org/10.1002/wcms.1327>.
- [34] D.A. Pantazis, X.-Y. Chen, C.R. Landis, F. Neese, *J. Chem. Theor. Comput.* 4 (2008) 908–919.
- [35] F. Neese, F. Wennmohs, A. Hansen, U. Becker, *Chem. Phys.* 356 (2009) 98–109.
- [36] F. Neese, *J. Am. Chem. Soc.* 128 (2006) 10213–10222.
- [37] F. Neese, *J. Chem. Phys.* 122 (2005), 034107/034101–034113.
- [38] Y.L. Ni, Q. Peng, C.M. Deng, X. Gao, Z.G. Shuai, *J. Phys. Chem. A* 114 (2010) 7817–7831.
- [39] B. Minaev, G. Baryshnikov, H. Agren, *Phys. Chem. Chem. Phys.* 16 (2016) 1719–1758.
- [40] G. Baryshnikov, B. Minaev, H. Ågren, *Chem. Rev.* 117 (2017) 6500–6537.
- [41] Q. Peng, Y.L. Niu, Q. Shi, X. Gao, Z.G. Shuai, *J. Chem. Theor. Comput.* 9 (2013) 1132–1143.
- [42] T. Lu, F. Chen, *Multiwfn: a multifunctional wavefunction analyzer*, *J. Comput. Chem.* 33 (2012) 580–592.
- [43] P.K. Samanta, D. Kim, V. Coropceanu, J.-L. Brédas, *J. Am. Chem. Soc.* 139 (2017) 4042–4051.
- [44] M.J. Leitl, F.-R. Küchle, H.A. Mayer, L. Wesemann, H. Yersin, *J. Phys. Chem. A* 117 (2013) 11823–11836.
- [45] H. Oberhofer, J. Blumberger, *Phys. Chem. Chem. Phys.* 14 (2012) 13846–13852.